Composite Structures 327 (2024) 117644

Contents lists available at ScienceDirect

Composite Structures

journal homepage: www.elsevier.com/locate/compstruct

Effects of fiber layout on strength and failure of 3D printed notched composites

Davide Battini [a,*], Luca Giorleo [b], Andrea Avanzini [a]

[a] Department of Mechanical and Industrial Engineering, University of Brescia, Via Branze 38, I-25123 Brescia, Italy
[b] Advanced Prototype Laboratory, Department of Mechanical and Industrial Engineering, University of Brescia, Via Branze 38, I-25123 Brescia, Italy

ARTICLE INFO

Keywords:
Composites
Additive manufacturing
Stress concentration
Notch
Carbon fibers
Failure

ABSTRACT

This study investigates the effect of printing strategies on the strength of additively manufactured notched fiber reinforced composite specimens. Specimens with varying notch geometries (two radii and two opening angles) and fiber layouts (unreinforced, unidirectional, quasi-isotropic and concentric) were 3D printed and tested under tension. Digital image correlation provided surface strain field data. Results showed that fiber deposition patterns significantly impact notch sensitivity, failure loads and mechanisms, with notch geometry being of secondary importance. The unidirectional layout achieved the highest strength but with progressive failure, while quasi-isotropic specimens failed abruptly from the notch. The concentric layout shielded the notch region but induced premature failure away from the notch due to transverse stress. Stress concentration factor approaches, which work well for conventional laminates, have limitations for 3D printed composites due to local differences and complex interactions. Optimizing fiber deposition, instead of geometry, emerges as a promising design route. Combining unidirectional and contouring algorithms may improve performance. However, further studies utilizing multiscale modelling and local failure analyses are needed to fully understand failure mechanisms and guide optimal notch designs for 3D printed composites. With improved understanding and design methods, 3D printing promises to unlock new possibilities for structurally efficient notched composite parts.

1. Introduction

3D printed composites materials have shown enormous potential for structural applications, thanks to the possibility to combine tailored mechanical properties with the complex shapes and fiber deposition patterns allowed by Additive Manufacturing (AM) technologies. Of course, local stress concentrations resulting from the presence of holes or other types of notches may reduce the mechanical performances of 3D printed parts, hindering the potential benefit of AM technology. Several studies have explored notch effects in 3D printed metals [1–3] and polymers [4,5,14,15,6–13], finding factors like print orientation and layer adhesion impact failure loads. However, research focused specifically on 3D printed composites materials has been more limited despite their relevance for structural applications. Moreover, most of this research focuses on open-hole notch configurations [16–19] and addresses technological aspects like hole contouring or drilling methods [16,17], or design considerations that exploit unconventional fiber patterns [18,19]. Nonetheless, the understanding around different fiber patterns and different non-open-hole notch geometries is still lacking and structures like metamaterials, lattices, biomimetic designed or topologically optimized parts, often include side grooves or notches.

Additively manufactured parts with geometrically discontinuous regions are not only associated with complex stress gradients, but their fiber layouts may be very different from what could be observed on their conventional composite counterparts with fibers following curved paths, fiber contouring notch edges and a mixture of different materials at notch tips.

Even when dealing with conventionally manufactured composites, the theoretical prediction of failure load for notched parts is inherently complex [20,21]. Analytical models have been developed and provide some strategies to predict failure in conventional notched laminates, including fracture mechanics [20,21], simplified stress criteria [22], the Theory of Critical Distances [23,24], a notch stress intensity factor formulation dependent on elastic properties and notch tip geometry [25,26] and more recently the Virtual Isotropic Material Concept [27,28]. However, directly applying these approaches to Fused Filament Fabrication (FFF) composites is challenging due to differences in fiber position and orientation around notches compared to conventional

* Corresponding author.
E-mail address: davide.battini@unibs.it (D. Battini).

https://doi.org/10.1016/j.compstruct.2023.117644
Received 14 April 2023; Received in revised form 19 September 2023; Accepted 21 October 2023
Available online 30 October 2023

manufacturing.

However, directly applying these analytical models to long fiber FFF composites is challenging. As schematically shown in Figs. 1 and 2, the position and local orientation of the fibers close to the notch tip is affected by the constraints of continuous filament deposition, as well as by the printing strategies to control fiber pattern, contour walls and raster orientations.

In addition, unlike traditional composites where elastic properties are often homogenized, using average material properties in the critical notch region of FFF parts is questionable. The heterogeneous fiber patterns hamper applying the previously mentioned methods. For example, notch blunting effects such as those reported in [20], where failure occurred away from the notch tip, can hardly be described by models postulating the existence of a characteristic process zone ahead of the tip controlling the failure.

For all of the above-mentioned reasons, numerical prediction of the failure loads in presence of a notch or identification of optimal fiber deposition strategy remains challenging. Overall, even if recently different Finite Element modelling approaches were proposed to account for peculiar behavior of 3D printed composites [29,30], gaps in understanding notch effects and failure modes still persist [31–38].

In this context, an experimental approach was adopted in the present study, aiming to ascertain the weakening effect of notches in 3D printed parts and gain insights on its correlations with fiber patterns/orientations and notch geometries.

In order to investigate failure modes and notch blunting effects, a notch contouring (CONC) printing strategy was compared with configurations having straight fibers along different directions. Moreover, fiber orientation may result in anisotropy of the elastic properties for the composites, which, in turn, affects both the strength in the loading direction and the stress concentration at the notch [39,40]. Two common layouts were considered to investigate how the degree of anisotropy may affect failure loads and modes: unidirectional (UD), in which material strength is maximum along loading direction, and quasi-isotropic (Q-ISO), which more closely represent an isotropic behavior, but with lower mechanical properties. Different notch geometries were also printed to assess tip radius and opening angle effects.

Overall, a total of 16 different configurations were tested: three different fiber layouts (UD, Q-ISO, CONC) and matrix material only, in combination with four notch configurations.

2. Materials and methods

The specimens were produced with the FFF printer Markforged Mark Two which makes use of a printing head with two separate extrusion nozzles: one for the polymeric matrix filament and one for the long-fiber reinforced filament. For specimen regions with continuous fiber reinforcement, a Markforged proprietary filament was used, consisting of several long carbon fibers embedded in a Nylon matrix acting as a binder. In specimen regions without continuous fiber reinforcement, another proprietary filament (ONYX™) was used, consisting of a Nylon resin filled with micro-carbon fibers. While the manufacturer does not disclose the exact composition of the filaments and the properties of their constituents, relevant information can be found in investigations reported in the current literature [41–43]. The printing process parameters are controlled using proprietary software (Eiger™), which offers two algorithms to manage fiber deposition paths, named Isotropic and Concentric, respectively. These algorithms enable controlling fiber placement by the angle or by following inner or outer walls with concentric loops. In the presence of holes, notches, and curvatures, they result in significantly different fiber paths.

Four types of specimens with a V-notch or U-Notch on both sides were printed, as shown in Fig. 1, by combining two opening angles, $2\alpha = 0^\circ$ and $2\alpha = 90^\circ$, and two notch tip radii, $\rho = 0.1$ mm and $\rho = 1$ mm. All the specimens were printed flat and consisted of a total of 48 layers, each with a thickness 0.125 mm. The bottom and top surfaces (floor and roof) of the specimen consisted of four layers of ONYX with solid infill alternating $\pm 45^\circ$ raster orientation, whereas the remaining 40 layers were all fiber reinforced. In all cases, the outer surface (i.e. contour walls) consisted of ONYX material only (with one 0.4 mm wall).

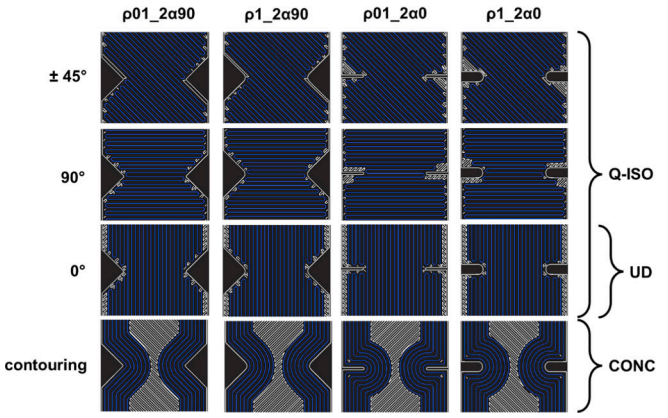

Fig. 2. Types of fiber deposition patterns in reinforced layers. The ± 45° orientation should also include a row with a mirrored fiber layout but was not reported to limit image size.

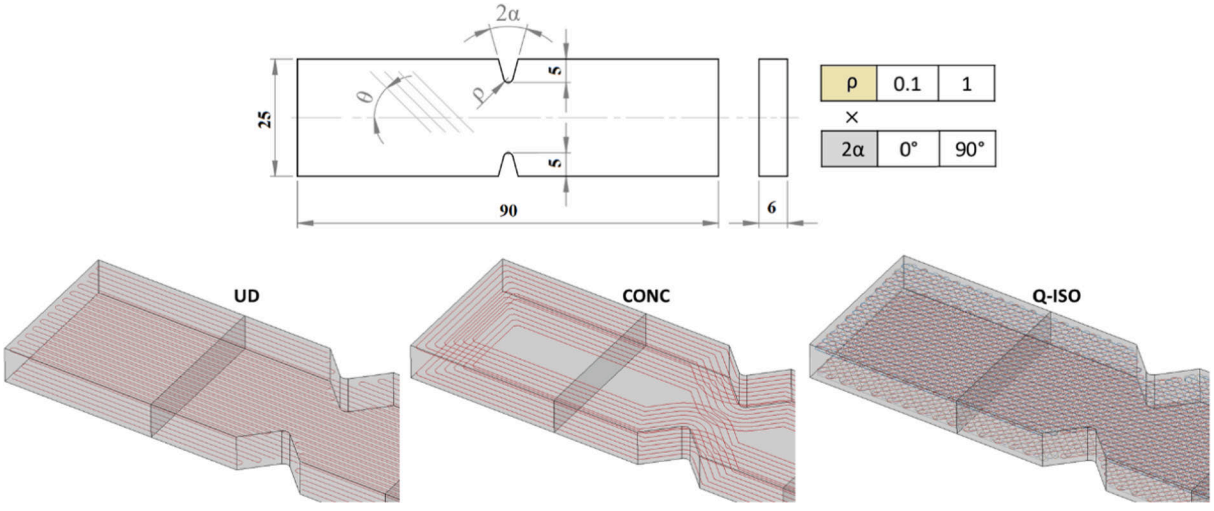

Fig. 1. Specimen geometries (dimensions in mm) and fiber paths (only first and last layer groups are shown).

Different reinforcement can be assigned to individual layers by changing the orientation angle θ or the deposition algorithm. In this work three different fiber layouts were considered, identified as UD (Unidirectional, $[0°]_{40}$, Isotropic algorithm), Q-ISO (Quasi-isotropic, $[0°/+45°/-45°/90°]_{10}$, Isotropic algorithm,) and CONC (40 layers, Concentric algorithm, 7 loops) (see Fig. 1). The number of loops for the CONC specimens was set to 7, the maximum number that allows for continuous deposition given this sample geometry. Increasing the number of loops would disrupt the contouring and not provide additional reinforcement in the central region.

UD and Q-ISO are common layouts chosen to investigate high and low degrees of anisotropy, respectively. In the UD configuration fibers are all aligned with the loading direction. In the Q-ISO configuration, fibers are arranged along four different orientations and layers with fibers at 45° and 90° should provide higher resistance to transverse splitting, with the predictable drawback of lower stiffness and strength compared to UD. The CONC layout allowed us to investigate the effects of notch contouring. In this case, some sort of beneficial effect should be evident due to the fibers following the notch contour, resulting in alignment with the maximum principal stress directions near the notch tip. The fiber patterns of each unique fiber layer (i.e. 0°, ±45°, 90°, concentric contouring) and notch configuration pair are shown in Fig. 2. As is evident, the presence of contour walls necessitates positioning fibers of a 3D printed long fiber composite further away from the notch edges and tips. Moreover, the continuous deployment of fibers results in their direction reversing upon reaching the walls (leading to "U-turns" in the fiber paths at walls) causing the presence of local matrix-only regions.

For each combination of fiber layout and notch geometry (i.e. UD, CONC and Q-ISO), three tensile tests were carried out. For each notch geometry three additional samples made with ONYX only were printed, for a total of 48 test samples. The specimens were subjected to tensile loading on a servo-hydraulic test rig (Instron 8501, 100 kN max load) with a constant crosshead displacement rate of 0.5 mm/min. The tests either ended at fracture, with physical separation in two parts of the specimen, or in presence of macroscopic cracking accompanied by drastic load decrease. For each configuration, at least one test included measurement of the strain field by means of Digital Image Correlation (DIC) to better identify critical regions and failure mechanisms. DIC measurements were carried out by means of a calibrated stereoscopic GOM Aramis configuration with two 6MP cameras (GOM Aramis 6 M), two blue light sources and polarizing filters mounted on each component. The stereoscopic recordings were processed with the GOM Correlate 2020 software. Depending on the speckle pattern size and quality, the facet size ranged from 13 to 17 pixels, and the center-to-center distance ranged from 7 to 10 pixels. In addition, analysis of variance (ANOVA) and Tukey range tests were performed on tensile tests results to evaluate the significance of fiber layout, notch tip radius, ρ, and notch opening angle, 2α, on the maximum force F_{max} recorded during each test. More specifically a first order triple-way ANOVA was carried out for the three reinforced families (UD, Q-ISO, CONC) while a second order two-way ANOVA was performed to analyze the ONYX family individually. Tukey range tests were instead used to visually inspect the differences of means among groups and subgroups. Despite the potential influence of the number of floor and roof layers on both the tensile test and DIC results, the default setting of 4 layers for solid infills was maintained. This decision was necessitated by the limitations of the proprietary slicing software, which precludes reducing this number to zero.

Finally, fracture surface analysis was also carried out via optical microscopy (LEICA DMS 300) and scanning electron microscopy (SEM).

3. Results

3.1. Tensile tests on ONYX specimens

The results of the tensile tests on ONYX specimens are summarized in Fig. 3(a) and (b) for the different configurations. The specimens showed good repeatability, particularly in the initial part of the force–displacement (F-dL) curve. However, a higher variability was observed for larger displacements as the material progressively sustained damage. The shape of the F-dL curve is similar for all cases, with an overall ductile behavior that reduces the sensitivity to variations of notch geometry.

The values recorded for peak loads on ONYX specimens are summarized in Table 1 (and in together with all the other tested families). By grouping the specimens with the same notch tip radius, a slight difference between the series with radius $\rho = 1$ mm and $\rho = 0.1$ mm can be appreciated. With a larger tip radius, the average peak load is higher, consistent with a lower stress concentration effect. Simultaneously, the standard deviation (STD) increases, suggesting that final failure is more influenced by the presence of internal defects rather than by stress concentration effects. Although this interpretation might seem assertive, a larger tip radius results in a lower notch effect, which causes internal defects to play a more critical role in the failure mechanisms [44]. Consequently, the random distribution of internal defect size and location may be causing the higher result scatter in configurations with reduced notch effects.

An ANOVA test on ONYX samples only was also carried out by considering a second order model (ρ, 2α, ρ·2α) and confirmed that the tip radius is the only significant parameter with a p-value of 0.018.

3.2. Tensile tests on long carbon fiber reinforced specimens

The results of tensile tests on long carbon fibers reinforced specimens are presented in Fig. 4. In general, despite the inherent heterogeneity of 3D printed composite materials, the results were quite consistent for each configuration and showed good repeatability. Among the examined configurations, UD showed a more progressive decay of mechanical strength and stiffness and, in most cases, was capable of sustaining higher load levels and larger displacements, with ultimate failure loads ranging from ≈ 25,000 to 31000 N. On the contrary, for CONC configurations the lowest peak load values were observed (from 6200 to 10000 N). During the test, no sign of layer failure due to fiber breakage could be detected and the shape of the F-dL resembled more that of a ductile material. Q-ISO specimens featured an intermediate behavior between UD and CONC in terms of stiffness and peak load values (from 16,000 to 20000 N). Overall, when comparing the ultimate load at failure for the different families, having all the fibers aligned in the loading direction allowed the UD configuration to exhibit the highest value.

On the other hand, while a progressive deviation from linearity was observed for all configurations, the failure mode and the damage progression varied significantly.

Representative failed specimens are shown in Fig. 5, which also include the ONYX series, where it can be better appreciated that the differences observed for the F-dL curves reflect the different failure modes elicited by each fiber layout.

Considering UD samples, evidence of layer damage could be noticed in several tests, both as audible "clicks" during the test, and as sudden jumps in the F-dL curve, but a fracture surface could not be generated, and macroscopic failures occurred by transverse splitting of the specimen along the longitudinal direction. The crack originated from the notch region and then extended across the entire specimen towards the grip area. Considering Q-ISO configuration, the most remarkable difference is that no progressive failure could be observed in this case. The specimens broke suddenly, with failure originating from the notch and propagating perpendicular to the loading direction, resulting in the specimen separating into two parts. For CONC specimens, while the

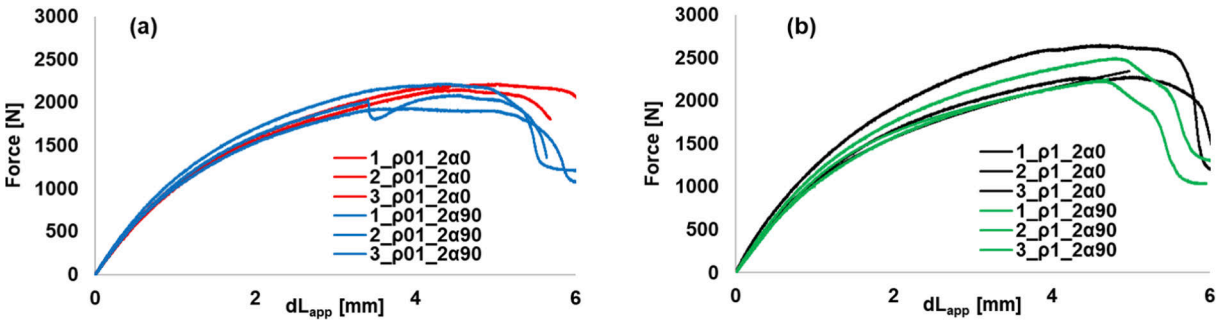

Fig. 3. Tensile tests on notched ONYX specimens (a) ρ01_2α0, ρ01,2α90, (b) ρ1_2α0, ρ1_2α90.

Table 1
Peak loads for tensile tests on notched ONYX specimens (values in N).

n	ρ01_2α0	ρ01_2α90	ρ1_2α0	ρ1_2α90
1	2215	2219	2650	2497
2	2150	2088	2280	2233
3	2179	1933	2343	2249
Average	2181	2080	2424	2326
STD	33	143	198	148
Average	2131		2375	
STD	108		165	

fibers effectively hindered the notch effect, failure occurred prematurely by transverse splitting in the central region of the specimen where fibers are not present. Even in the presence of large central fissures in the material, CONC specimens did not physically break because the concentric fibers along the notch contour remained intact. However, the positive reinforcing effect of the contouring fibers could not be fully exploited.

3.3. ANOVA and Tukey range test on the peak tensile loads

Both the ANOVA and the Tukey range test for peak tensile loads clearly indicated the fiber layout as the only significant parameter. Specifically, the ANOVA led to the following p-values: 0.705, 0.568 and < 0.001 respectively associated with the opening angle, 2α, the tip radius, ρ, and fiber layout. The Tukey test range reinforced what was already evident from the ANOVA by showing that the only significant mean difference is over different fiber layouts as can be seen in Fig. 6. Each tensile test is represented with a red cross and the average across each fiber layout with a dotted black line. The Tukey test range was performed with a 95 % confidence interval and only groups with a significantly different mean are shown in the table.

Both the ANOVA and the Tukey range test findings mentioned above are consistent across all the examined configurations. They are in line with the strain field and failure modes analyses reported in the following sections, suggesting that the fiber layout is the dominant factor. After introducing the long fiber reinforcement, the effect of the tip radius (seen for ONYX specimens) lost its significance and no trend related to notch geometry can be seen in Fig. 6 when looking at each reinforced family.

3.4. DIC analyses of strain fields

The following sections report the maximum principal strain fields for all the different reinforcement families and notch geometries. For comparison purposes, three values of applied displacements dL_{app} (0.167 mm, 0.5 mm and incipient failure) were chosen to cover the different phases of progressive deformation for all specimens including: 1) the initial stage, when the load is low and the material is not yet damaged, 2) an intermediate phase, in which the strain field is fully

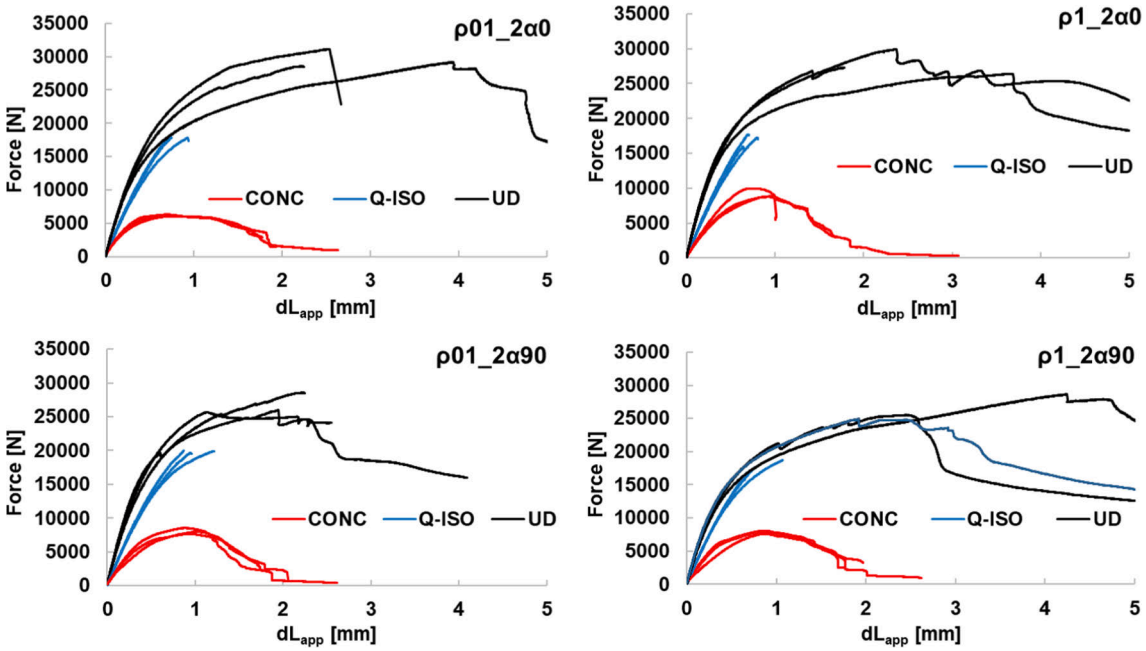

Fig. 4. Tensile tests on notched fiber reinforced specimens.

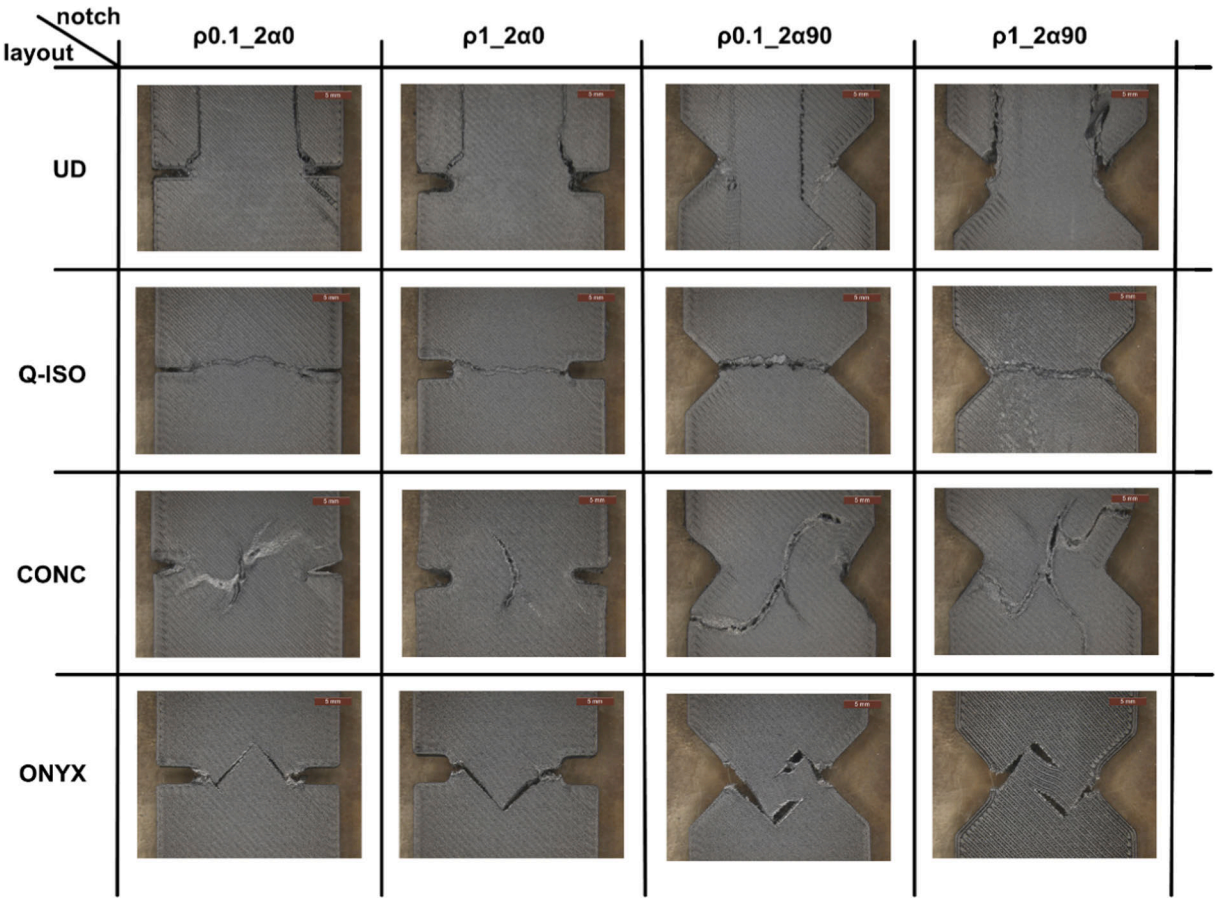

Fig. 5. Failed specimens.

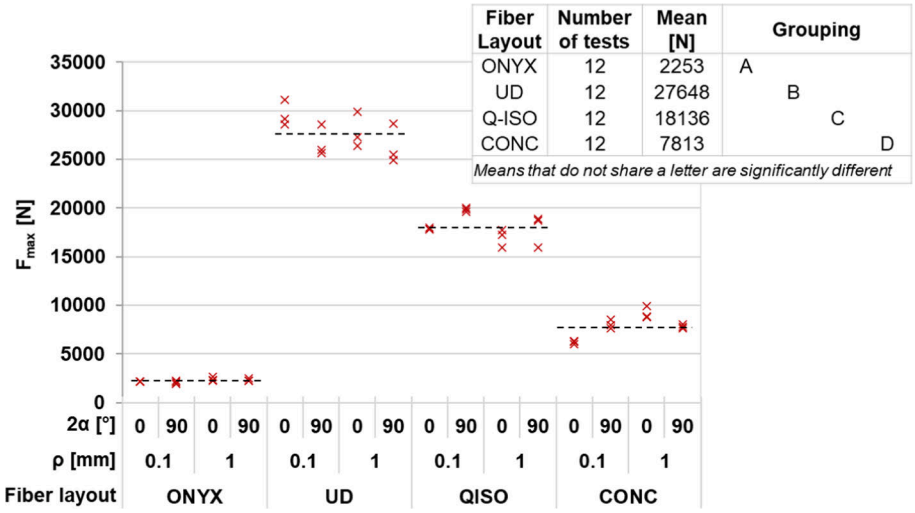

Fig. 6. Peak tensile loads data and Tukey test range grouping.

developed and 3) a final phase when specimens were about to fail. In general, both the strain fields and the macroscopic failure sequence were similar across the different geometries and were mostly dependent on the fiber layout as was already proven by the ANOVA analysis. Moreover, and coherently with the ANOVA analysis, the notch radius significance of ONYX samples translates into slightly lower strain levels for $\rho = 1$ mm.

However, it should be noted that DIC measurements refer to surface fields, and the presence of roof/floor layers might affect the results. Nonetheless, appreciating core deformation/failure is hardly possible unless (for example) using micro-CT and Digital Volume Correlation, and DIC results still allowed for the overall failure mode interpretation.

3.4.1. *ONYX samples*

Considering ONYX samples, the deformation fields observed around the notch are in line with expectations despite the material not being perfectly homogeneous, isotropic and elastic. As shown in the sequence of DIC images in Fig. 7, higher values of maximum principal strains are

present close to the apex of the notch and, as the load increased, a localized strain concentration developed ahead of the tip until a crack nucleated and started propagating. Strain gradients are also shown along raster orientations lines, indicating possible favorable crack propagation paths. In fact, after contour wall breakage, the fracture usually propagated along a 45° degrees inclined direction with respect to load and specimen axis, apparently following the raster orientation of the surface layer (see Fig. 5). This behavior is also in line with [33] where XYZ ± 45° samples showed the same strain concentration along the ± 45° directions at the notch tip followed by a propagation along the raster orientation.

3.4.2. Q-ISO samples

As shown in the sequence of DIC images reported in Fig. 8, Q-ISO samples also exhibited a strain concentration close to the notch apex, but the location of the region in which the highest strains are present varied depending on the notch geometry.

When the $\rho = 0.1$ mm and $2\alpha = 0°$ configuration is considered, the peak principal strains are initially located above and below the apex, running parallel to the notch contour wall, which in this case is normal to the loading direction. This phenomenon can be attributed to a slight over-extrusion of the filaments (visually inspected), paired with the null opening angle and very small tip radius of this notch geometry, which caused micro-adhesions of matrix material along the notch edges, in particular for the roof and top (unreinforced) layers. This determined a local perturbation of the strain field, which is only noticeable for small values of $dL_{app.}$ For higher loads this effect gradually disappeared and did not affect the failure modes.

When the other configurations are considered the peak principal strains are located ahead of the notch apex, at the end of the notch fillet, as could be expected. When the load increased, the extension of the region with peak strains also increased.

At failure, the maximum strain localized ahead of the crack tip and a crack nucleated in this region, followed by a sudden propagation perpendicular to the loading direction that separated the specimens in two parts (from tip to tip, as seen in Fig. 5). In general, the failures were less progressive than the other configurations examined, with DIC recording showing the specimens going from a no visible crack state to a fully cracked state within one frame (corresponding to an applied displacement increment lower than 0.01 mm). As also suggested by the shape of the load–displacement curves, the overall strain levels (Fig. 8) were lower than those of other families and so was the strain at failure. In fact, the final failure likely coincided with the first ply failure occurring in 0° layers when the fibers broke.

3.4.3. UD samples

As shown in the sequence of DIC images reported in Fig. 9, UD samples displayed a different type of strain field evolution and, consequently, of failure mode when compared to ONYX or other fiber reinforced families.

The maximum principal strain had a peak at the end of the notch fillet, as this region close to the tip lacks reinforcement because of the technological constraint of continuous fiber deposition (see Fig. 2 and Fig. 11). The cracks started at a 45° orientation (thus normal to the contour) but then propagated parallel to fibers (i.e. 0° orientation), as can be evidently seen in the incipient failure frames of Fig. 9. The crack propagation direction also corresponds with the two longitudinal bands affected by a strain gradient (from test start to end) running across the whole specimen length and being tangent to the notch tips. In fact, these bands show the highest strain values after notch tip regions. Similarly to Q-ISO, when the $\rho = 0.1$ mm and $2\alpha = 0°$ configuration is considered, the peak principal strains are initially situated both above and below the notch, running parallel to the contour wall. Again, this can be regarded as an effect of micro-adhesions between the notch edges, combined with the absence of fiber reinforcement in the contour, since in this area the fibers revert their path.

3.4.4. CONC samples

As shown in the sequence of DIC images reported in Fig. 10, CONC samples exhibited an entirely different type of strain field evolution, with a complete shielding of the notch effect and with the crack propagating from the highly stretched central region.

From the very initial stage of loading, two mirrored, crescent-shaped areas at the center of the specimen were subjected to high strains. These regions follow the curvature of the innermost concentric fiber path, thus being located at the boundary between the central matrix-only domain and the long-fiber reinforced domain (see Fig. 2 and Fig. 11). The crack originated in this area and then propagated following the circular path

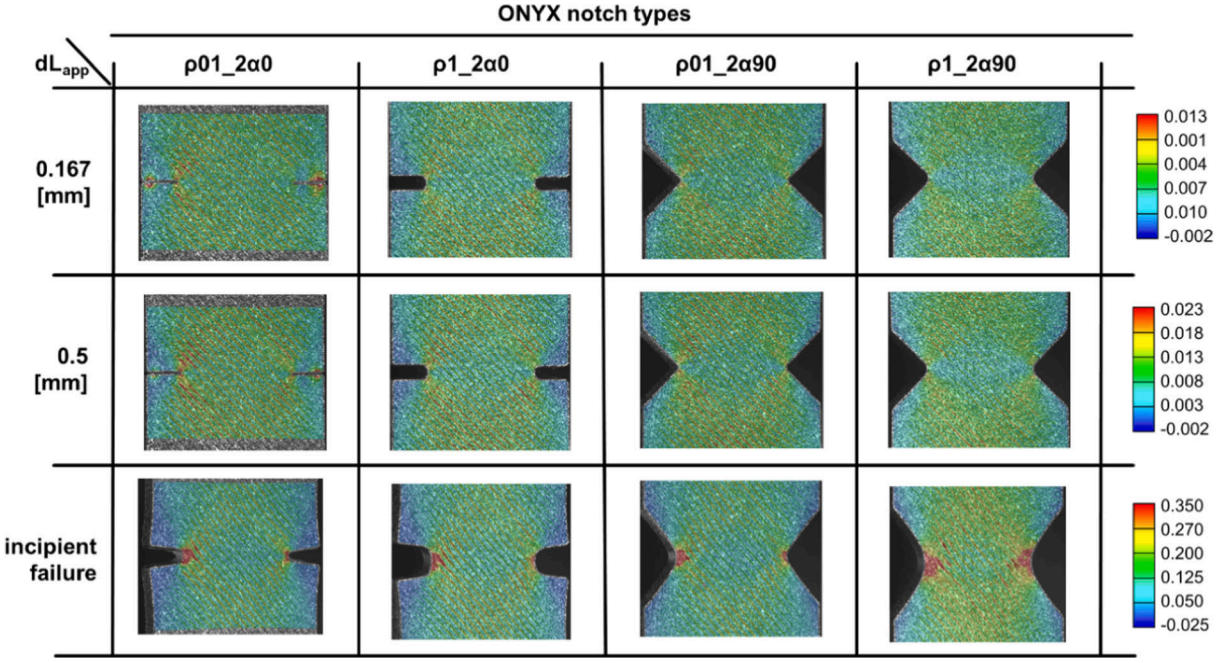

Fig. 7. Maximum principal strain on ONYX samples, respectively from left to right: ρ01_2α0, ρ1_2α0, ρ01_2α90, ρ1_2α90.

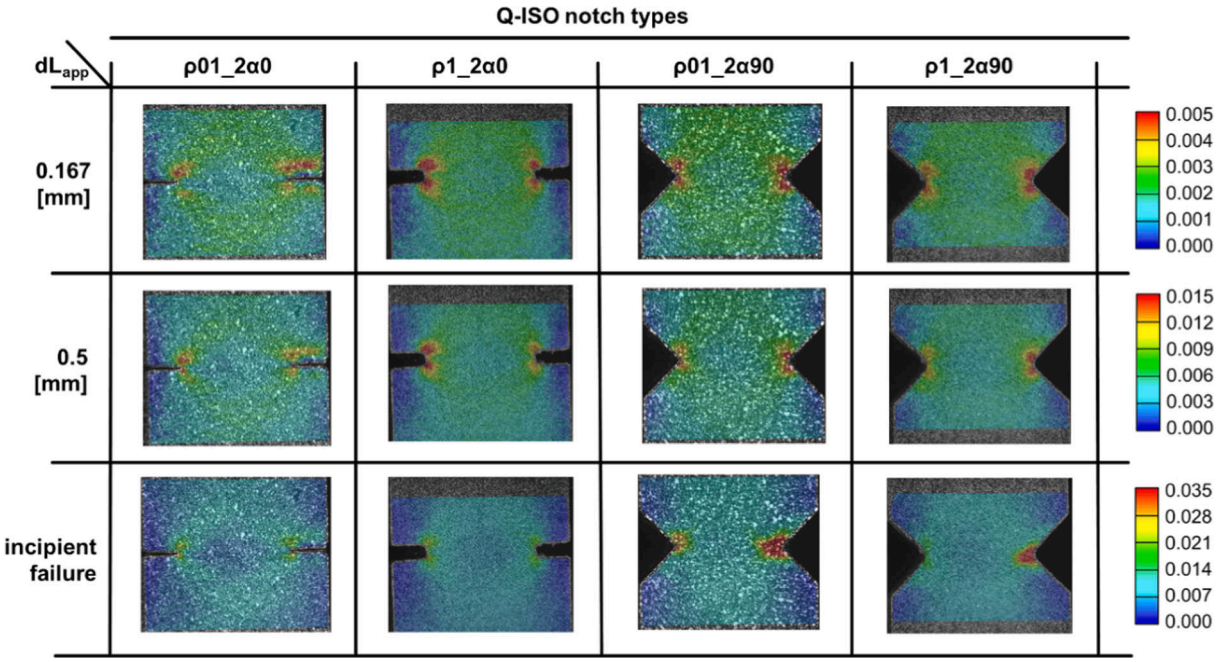

Fig. 8. Maximum principal strain on Q-ISO samples, respectively from left to right: ρ01_2α0, ρ1_2α0, ρ01_2α90, ρ1_2α90.

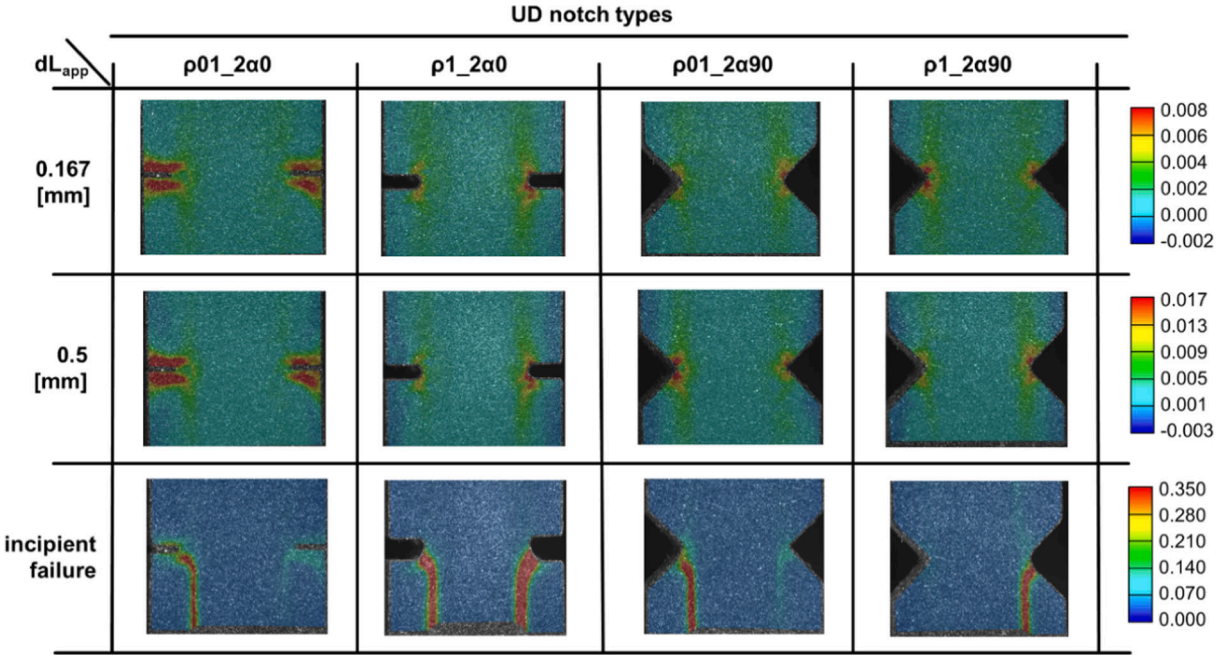

Fig. 9. Maximum principal strain on UD samples, respectively from left to right: ρ01_2α0, ρ1_2α0, ρ01_2α90, ρ1_2α90.

of the innermost fiber loop, initially nearly aligned with loading direction and then progressively more in the transverse one, pointing towards the outer walls, where the crack propagation was further deviated by the longitudinal fibers. Load bearing capability is progressively reduced the more the central crack opens. Despite macroscopic damage, no final separation into two pieces could be achieved, but for some configurations the cracks also extended to the fiber regions close to the notch tip.

4. Discussion

4.1. *Influence of printing strategy on failure mechanisms*

The comparison among the different examined configurations provides some interesting insights on the behavior of 3D printed composites in presence of a notch, in particular on blunting effects and failure mechanisms determined by fiber deposition patterns.

Fig. 11 depicts a representative example, specifically the ρ1_2α90 configuration.

Fig. 11(a) overlays the maximum principal strain directions (indicated by black arrows) and DIC contour maps onto the underlying fiber

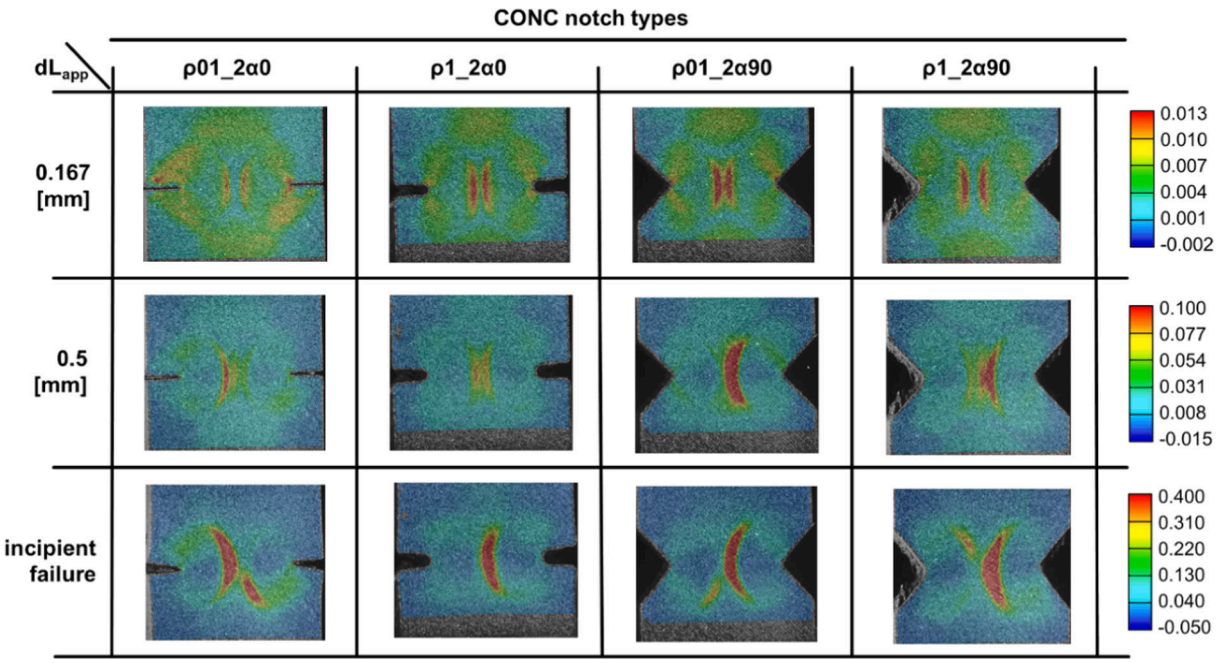

Fig. 10. Maximum principal strain on CONC samples, respectively from left to right: ρ01_2α0, ρ1_2α0, ρ01_2α90, ρ1_2α90.

deposition paths (represented by white lines, which correspond to the matrix deposition lines for the ONYX family). Fig. 11(b) shows instead the longitudinal and transverse strain components (i.e. e_L and e_T) across the tip-to-tip section. In the case of UD samples, the peak principal strain e_1 is located in a region rich in matrix material. This is a result of the printing algorithm that cannot place the unidirectional fibers close enough to the notch tip. Additionally, two significantly deformed longitudinal bands, tangent to the notch tip, are noticeable. These run across the whole specimen and are clearly coincident with the intermediate region between two parallel fiber deposition paths. Along such bands, the maximum principal direction deviates from the loading direction and almost reaches 45° indicating that shear strains are also not negligible when compared with longitudinal and transverse ones. Both e_L and e_T are positive and have similar values, which confirms that as the specimen stretches along the loading direction, the middle section is concurrently stretching in the transverse direction. It can be concluded that the higher number of long fibers aligned with the loading direction is quite effective to enhance the ultimate load bearing capacity, by hindering cracks that would propagate transversely from the notch. This effect is less noticeable for the initial damage phase because, as already discussed, the fibers are placed at some distance from the tip.

For the Q-ISO samples, the directions of maximum principal strain are more similar to what could be expected for an isotropic material, and, in the initial stage, the strain localization was close to the notch tip, again in a region that lacks reinforcing fibers at 0° because of the printing strategy. The crack originated at the center of the tip and was fully oriented transversely for all the specimens. The maximum principal strain direction map is very different from the UD and the Q-ISO specimen is mostly stretched uniaxially along the loading direction. In particular, the transverse strain is negligible, due to the presence of 90° plies (±45° might also help), and the 0° plies are not sufficient to deviate the crack path. Most likely, when the fibers of these layers broke, the whole specimen failed.

In the case of the CONC samples, the fibers follow the contour of the specimen, resulting in fiber orientations around the notch that are closer to the principal stress directions expected ahead of the tip. As already mentioned, this should help them bear more load, without the drawback of the "U-curved" fiber ends in the notch region that can be seen in UD and Q-ISO. The contour map of e_1 clearly confirms that this fiber deposition strategy resulted in a sort of shielding effect around the notch and prevented failures originating from the tip. Unfortunately, when fibers are placed along the contour of the notch, they are exposed to a bending action caused by the axial load. This lever effect tends to straighten the curved fibers, so that while excessive deformation in the notch region is prevented, the central region of the specimen undergoes much higher strain levels, leading to premature crack nucleation. The crack then propagated along the innermost fiber loop until final tearing. Indeed, the tip-to-tip strain curves show the transverse strain (e_T) being dominating and almost coincident with the maximum principal (e_1) one for the most part. This peculiar behavior suggests that to take advantage of the blunting effect associated with notch contouring strategy, further optimization is necessary to avoid collateral effects on the overall strength, for example by combining the use of Isotropic and Concentric printing algorithms for different layers or even within the same one.

Finally, Fig. 11 also includes a representative ONYX sample. As for the Q-ISO samples, ONYX tip-to-tip strain curves. show that the longitudinal strain (e_L) is dominating, with negligible shear. Transverse strain behavior is instead different with respect to Q-ISO, and mostly related to Poisson effect except for the notch tip proximity. Crack started at the tip center with a roughly 90° orientation. Crack propagation was slower and, as previously mentioned, apparently followed the 45° angle of the outer layers raster orientation boundaries (white lines in Fig. 11(a)).

For a comparison with existing literature on conventional U and V notched composites, the limited number of papers related to these specific configurations restricts a comprehensive analysis. As observed in [24], "The preponderance of results on holes and cracks is most likely due to the applications to which composite laminate sheets are put.". Nevertheless, interest in side-notches arises more naturally when considering the complex shapes allowed by AM technologies. Some experimental results reported in [24] for CF/epoxy laminates and quasi-isotropic configurations with sharp or round side notches showed a notch stress concentration factor, K_t, up to 4.78. Differently from the current study, specimens displayed near-linear behavior up to failure, but damage mechanisms were not discussed. On the other hand, [28] investigated central notches with a V-Type tip, reporting evidence of notch-induced delamination, matrix cracking, and fiber breakage, but only for a glass-fiber laminate. However, given the inherent differences between AM and conventional composites, direct and detailed

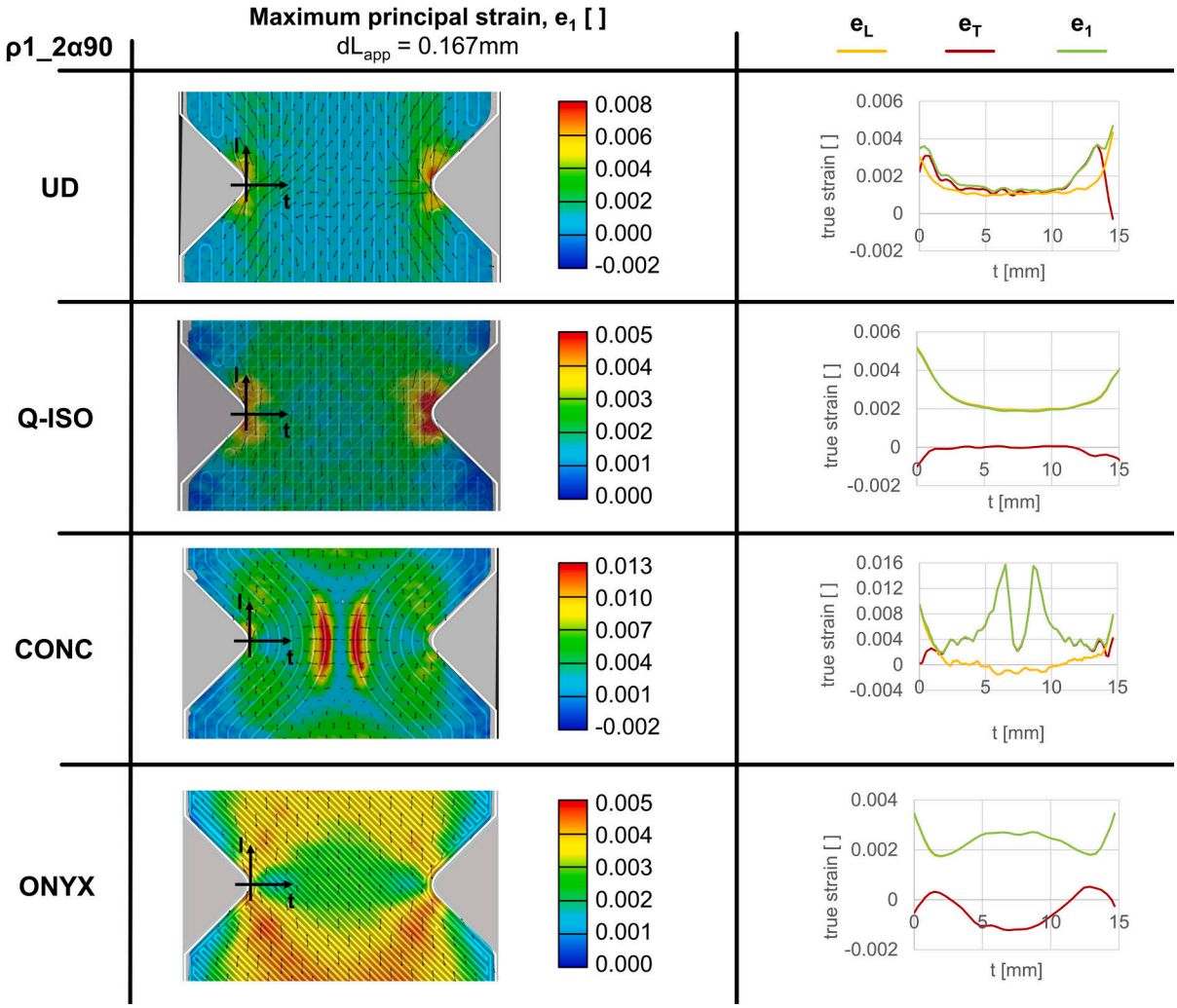

Fig. 11. (a) Maximum principal strain maps at 0.167 mm dLa_{pp} for the ρ1_2α90 specimens with superimposed fiber deposition path. (b) Longitudinal strain (e_L), Transverse strain (e_T) and Maximum principal strain (e_1) components along the net section (tip-to-tip).

comparisons between their structural behaviors would necessitate using the same type of specimen geometry, fiber/matrix materials, and fiber/matrix layouts.

4.1.1. Notch tip opening displacement

In order to have a rough estimation of the blunting effect and to allow for a qualitative comparison of the tip opening for different fiber layouts, the following approach has been adopted.

The $\rho = 1$ mm and $2\alpha = 0°$ geometry was chosen for the calculations and a tip opening distance, e_D, was defined as shown in Fig. 12. The offset distance was necessary to move away from the notch edges and allow a correct processing via DIC.

The tip opening distance results are presented as percentage change in length, $\Delta e_D = 100 \cdot (e_D - e_{D,0})/e_{D,0}$. Their trends are in line with the

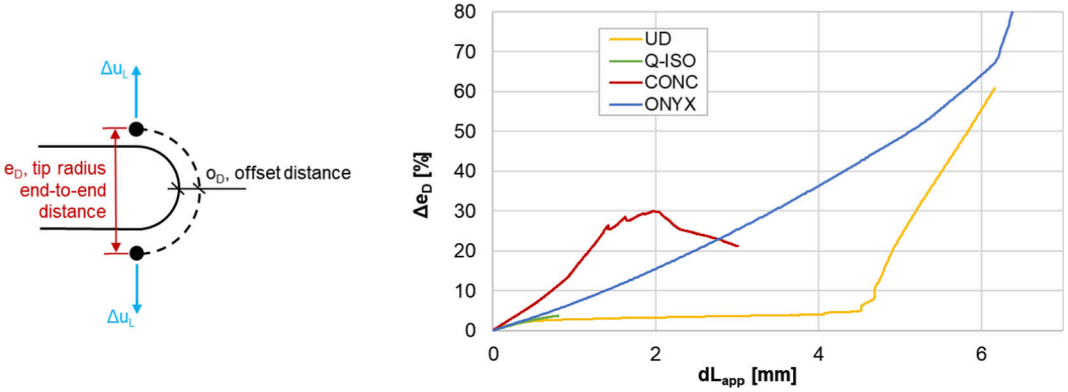

Fig. 12. Tip opening distance e_D calculations for the ρ1_2α0 specimens. The distance is defined at radius ends and results are reported as length change: $\Delta e_D = (e_D - e_{D,0})/e_{D,0}$.

failure mechanisms and strain fields commented in the previous section. When small displacements are applied to the specimens, the macroscopic behavior of the tip geometry (i.e. Δe_D trend) is equivalent for all the fiber layouts but the concentric one. This difference can be attributed to the effect of the curved paths of the concentric fibers, which tend to straighten the notch geometry and shift the maximum stress away from the tip. This is similar to what one might expect if the fiber paths were acting like truss-like elements with minimal bending stiffness. This is also the same behavior described as "lever effect" in the previous section.

Conversely, the Onyx sample is unique in achieving higher Δe_D values due to its significantly greater plastic deformation around the notch tip. The UD sample is almost stabilizing after applying more than 0.25 mm displacement because all the central fibers become fully engaged causing the notch to almost stop opening. Significant deviations in Δe_D trends at extremely high applied displacements, regardless of the fiber layout, are associated with the initiation and propagation of macroscopic cracks, leading to complex load transfers across the specimens.

4.2. Fracture surfaces and failure mechanisms: SEM analyses

As previously noted, the variations in fiber deposition patterns led to diverse failure modes which were clearly observable by visual inspection and DIC analysis. Since the fiber layout was the main factor affecting the failure process, a single geometry was considered ($\rho = 1$ mm, $2\alpha = 0°$) for the following fracture surfaces analyses. An initial distinctive feature, as depicted in Fig. 13, is that failure occurred along different planes, either normal, parallel, or inclined relative to the load, or even along the interface of fiber loops. Furthermore, not every sample could be divided into two parts, necessitating the exposure of fracture surfaces by cutting the segment of the sample outlined by the white dotted line in Fig. 13, where images taken with the optical microscope are also presented. Fig. 14 and Fig. 15 show fracture surfaces as observed with SEM at different magnifications either in the central area or in detailed sections of selected areas. Generally, failure types were either intralaminar or cross-laminar, with no apparent evidence of delamination caused by interlaminar stresses.

As already discussed, for UD samples, the crack started from the notch and initially propagated along an inclined direction (approximately 45°), then parallel to the specimen axis. In the first region, the specimen mainly consists of matrix material due to the presence of the contour wall. As a result, a ductile failure of the matrix occurred, creating a very rough and irregular surface (Fig. 14 UD a). Notably, in this area where the fibers are curved to accommodate a reversal in deposition direction, some broken fibers are observable (Fig. 14 UD b). On the other hand, the fracture surface of the second region (Fig. 15 UD) is very flat. Here a cross-laminar failure is evident, where the front of the crack propagated across the laminae by shear failure of the matrix in the binding polymer-rich area at the interfaces between adjacent fiber paths. In this section, the fibers, still embedded in the matrix and undamaged, allowed the specimen to withstand higher ultimate loads at failure. Locally, a few exposed longitudinal fibers are visible, along with small cavities potentially generated by the expansion of local pores (Fig. 15 UD b,d). The Q-ISO samples fractured normally to load direction, with failure initiating from the notch tip (Fig. 14 Q-ISO a). Similarly to what reported in [32,35], the layered structure can be clearly noticed (Fig. 13 Q-ISO c, Fig. 15 Q-ISO a), as well as the different failure mechanisms depending on each layer orientation. The 90° layers (i.e. with fibers perpendicular to loading) show matrix failure, with significant matrix deformation and evidence of local debonding (Fig. 15 Q-ISO b,c,d), as a consequence of stress acting normal to the local fiber axis. As shown in Fig. 14 Q-ISO b, at the border of the layer, where the fibers are instead curved to allow for continuous deposition, fibers failure can instead be appreciated. Most of the fiber breakage however, is evident in the 0° and the ± 45° layers (Fig. 15 Q-ISO c,d) where fiber pull-out can also be noticed (especially for the 0° layers). For the CONC specimen, the fracture originated at the center of the sample with limited damage to the fibers. This area can be observed in Fig. 15 CONC a,b, where the presence of fibers still partially embedded in the matrix can be noticed. The fracture propagated at the interface between the inner fiber loop and the Onyx infill. Similarly to UD, the failure occurred in the matrix but this time it was caused by normal stress (with respect to the local fiber direction) rather than shear. In fact, the surface is rougher (Fig. 15 CONC c), matrix fibrillation is evident and a debonding of the outer fibers is also noticeable (Fig. 15 CONC d). Fig. 14 CONC a,b shows details

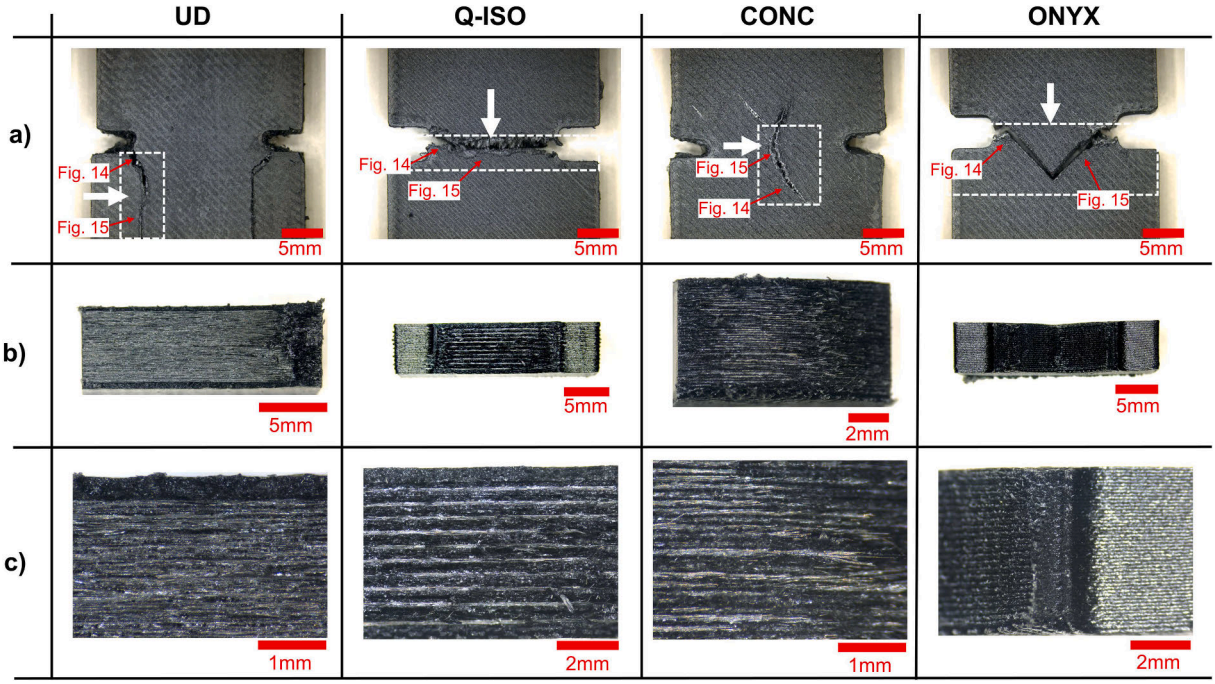

Fig. 13. Position of examined fracture surfaces of the samples.

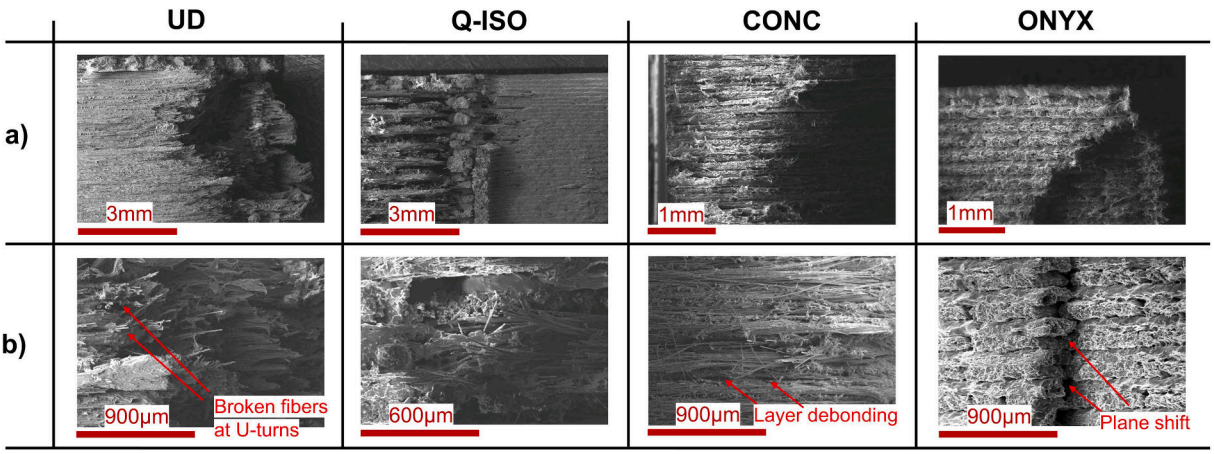

Fig. 14. Details of fracture surfaces close to the notch tip at SEM.

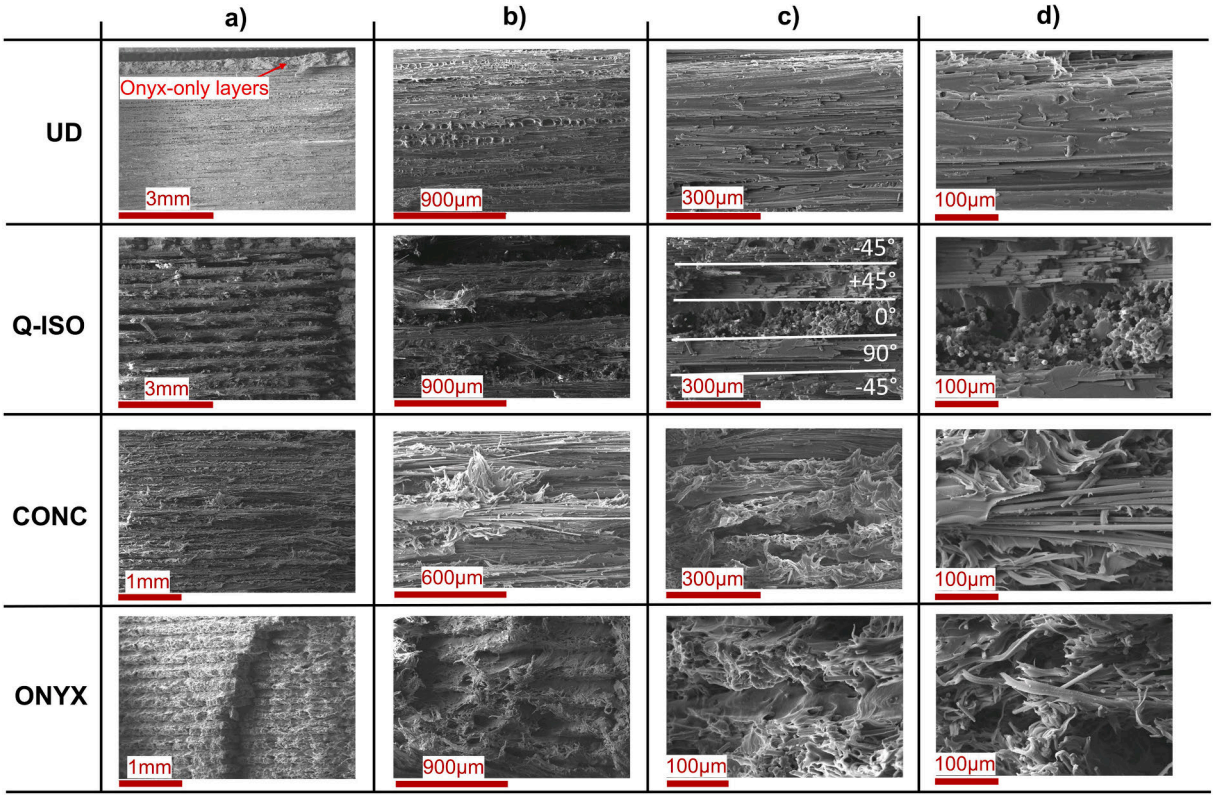

Fig. 15. SEM images of fracture surfaces at different magnifications.

closer to the crack front where some evidence of incipient delamination between the layers can be noticed, as well as more extensive fibers debonding. Finally, the Onyx samples showed a V-shaped fracture surface with failure starting from the notch (Fig. 13 ONYX a). The fracture surface aligns with observations noted in [33]. The area presents a rougher appearance, demonstrating matrix fibrillation (Fig. 15 ONYX a, b,c), and short fibers pullouts (Fig. 15 ONYX c), with the layered structure of the material still clearly discernible. Failure propagated by breakage of successive filaments and, in the specimen under examination, shifted to parallel planes (Fig. 14 ONYX a,b), possibly because of the presence of local defects caused by filament deposition and because of macroscopic changes in load transfer caused by advanced damage.

4.3. *Influence of fiber layout and notch geometry on stress concentration*

One of the goals of the present study was to investigate the weakening effect of notches in 3D printed parts for different combinations of notch geometry and printing strategy. To this aim, the examined configurations differed significantly in terms of the degree of anisotropy (UD and Q-ISO) or the adoption of a notch contouring strategy (CONC). The notch geometries included both sharper (i.e. ρ01_2α0) and milder (i.e. ρ1_2α90) configurations.

The anisotropy of composite materials is clearly dependent on the orientation of the fibers in each layer. The more the fibers are aligned with the loading direction (0° angle), the more the stiffness and the strength in that direction will increase. On the other hand, when a notch is present, the related stress concentration is also affected by the degree of anisotropy [27]. The theoretical stress concentration factor of

orthotropic notched plates (K_{t_ortho}) under tension, which accounts for different types of side grooves, can be calculated using the formula given in [32] (eq. (1):

$$K_{t\_ortho} = 1 + \frac{\zeta}{2}\left(\widetilde{K}_t - 1\right)\# \tag{1}$$

Where $\widetilde{K}_t$ is the stress concentration factor for the isotropic case and the same notch geometry, and the coefficient ζ, defined as per eq. (2):

$$\zeta = \sqrt{2\sqrt{\frac{E_1}{E_2}} - 2\nu_{12} + \frac{E_1}{G_{12}}}\# \tag{2}$$

quantifies the degree of anisotropy as a function of the elastic constants E_1, E_2, ν_{12}, G_{12} in the principal elastic reference system. The application of this approach to several types of notches under tension, showed that the stress concentration factor increased with the degree of anisotropy. Consequently, for a notched member made of orthotropic material, the failure load will result from the balance between two contrasting effects, the increase of strength associated with higher unidirectionality, and the higher K_{t_ortho}. As noted in [32], the extension of this approach to homogenized orthotropic laminates is also possible, but subject to some limitations. In fact, the maximum stress determined does not necessarily correspond to any of the actual maximum notch stresses occurring in the different plies of a multi-directional laminate and edge effects are not considered. Although the unique characteristics of 3D printed composites may cause some deviations from the ideal case, it is worthwhile to explore if this approach can provide valuable insights into the current scenario, particularly for UD and Q-ISO configurations where the fiber layout closely mirrors that of traditional laminates.

In a previous study [31] the mechanical properties of the same type of 3D printed orthotropic laminae were characterized and the properties along longitudinal (L) and transverse (T) directions were determined ($E_L = 67570$ MPa, $E_T = 1200$ MPa, $G_{LT} = 428$ MPa and $\nu_{LT} = 0.33$). In the same work, tests conducted on plain samples showed that neglecting the contribution of roof and bottom layer made of polymeric material only, the Ultimate Tensile Strength (UTS) of a UD composite was about 815 MPa, whereas for a Q-ISO layout, based on the sequence [0/45/-45/90], UTS was reduced to about 400 MPa. Using well established methods based on Classical Laminate Plate Theory [33], the effective elastic properties of the UD and Q-ISO laminates investigated can then be calculated, yielding values of the coefficient ζ of 4.08 for UD and 2.00 for Q-ISO, as per eq. (2). The stress concentration factor for isotropic material $\widetilde{K}_t$ can also be evaluated for each configuration using the formulae reported in [45] for plates with double sided U or V grooves. The theoretical stress concentration factors of the orthotropic notched plates can finally be determined with eq. (1). As depicted in Table 2, the values of K_{t_ortho} vary significantly, depending on the combinations of notch geometry and fiber layout.

Based on these data, the theoretical load level F_{th} for which the peak stress at the notch reaches the UTS value can be estimated as per eq. (3):

$$F_{th} = \frac{UTS}{K_{t\_ortho}} A_L\# \tag{3}$$

Where A_L is the net area of the cross-section at the notch, again considering fiber reinforced layers only.

For the present case, the theoretical predictions indicate that the tip radius is the dominating factor, expecting a significantly larger reduction in strength when ρ = 0.1 mm. On the other hand, the advantage of using UD laminates, despite the higher strength in the loading direction, should be limited because the UD K_{t_ortho} is almost twice the Q-ISO one. Taking experimental evidence into account, the values of F_{th} are considerably below the ultimate failure loads of the tested samples, which, as noted earlier, are notably higher for UD. Moreover, ANOVA analysis of experimental results showed that fiber layout is the dominant factor for ultimate failure load. On the other hand, from a design point of view, F_{th} should be regarded as the theoretical load associated with first occurrence of some damage at the notch. Although the F-dL curves do not explicitly indicate macroscopic damage at F_{th} load levels, it's noteworthy that in several configurations, the UD specimens exhibited sudden, macroscopic jumps at load levels below UTS and, in some cases, similar to or only slightly higher than Q-ISO failure strength. Beyond this load level, up to ultimate failure load, the strength of the notched composite depends on whether stress redistribution will occur and on the failure mechanism that leads to final failure. However, one should note that a precise quantitative interpretation is also limited by the fact that the current theory is valid for a linear elastic behavior and while the fully reinforced rectangular strips tested in [30] showed a linear response up to failure, the current notched specimens definitely show more non-linearity.

The distinctive characteristics of 3D printed composites complicate the correlation of these theoretical values with ultimate failure loads when a notch is present. First, at the notch side locations, the continuous deployment of the filament in which the fibers are pre-embedded causes the fibers to follow a highly curved U-shape, which is necessary to revert the motion when approaching the contour lines (see Fig. 2). Therefore, near the notch edges, the effective local direction of the fibers is significantly more complex than in traditional laminates. Moreover, while using standard contour walls enhances the accuracy of a 3D-printed geometry, it results in matrix material at the notch tip, which positions the fibers at an offset distance from the most stressed area. As can be appreciated in Fig. 16, imperfect merging between outer contour and inner fiber reinforced filaments may also result in highly detrimental presence of voids [31,32], which will act as preferential crack initiation sites when load is applied. Additionally, due to their nature, such defects also (and mostly) end up at geometric discontinuity or high curvature locations which are especially unfavorable as these usually correspond to the most stressed regions.

Further differences with conventional laminates are that, for FFF composites:

- The matrix material itself may also exhibit some anisotropy, due to raster orientation and/or presence of short fibers in the filament.
- In currently available commercial printers, fibers are embedded in thermoplastic material, not in the more common thermoset resins.
- The achievable fiber volume fractions are lower than conventional composites (about 35–40 % [30]).

Consequently, especially for composites with limited amount of unidirectional 0° layers the overall behavior tends to be more non-linear, even under lower loads.

Overall, comparisons with test results suggest that methodologies based on stress concentration factors, developed for ideal orthotropic plates with homogenized properties, face limitations when considering the UTS of 3D printed composites. The counterbalancing effect of anisotropy on strength and stress concentration factor could be partially appreciated only when considering the initial damage condition. A further observation is that the results for the CONC configuration can hardly be interpreted in the framework of theories based on stress concentration effects only.

Table 2
Stress concentrations factors and theoretical failure loads.

	$\widetilde{K}_t$	K_{t_ortho}		$F_{th,UTS}$ [N]	
		UD	Q-ISO	UD	Q-ISO
ρ0.1_2α0	9.35	20.9	11.0	2927	2718
ρ0.1_2 α 90	6.69	12.6	6.69	4846	4482
ρ 1_2 α 0	3.22	5.53	3.22	11,048	9312
ρ1_2 α 90	3.25	5.60	3.26	10,908	9212

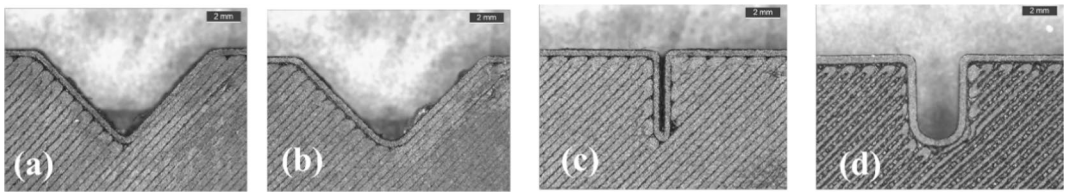

Fig. 16. Specimen top surface (a) ρ01_2α90, (b) ρ1_2α90, (c) ρ01_2α0, (d) ρ1_2α0.

5. Conclusions

Understanding the complex interactions between notches, stress state, and fiber orientation is crucial for optimizing structural performance of 3D printed composites [31]. To this aim, the current study investigated the effect of printing strategies on the strength of additively manufactured notched composites.

Results showed that fiber deposition patterns drastically influence notch sensitivity and failure modes. Despite variations in notch geometry, failure loads and mechanisms were dictated primarily by fiber layouts rather than notch shape. The UD fiber layout delivered the highest strength with failures occurring through progressive matrix damage and longitudinal splitting. The tensile loads did not ultimately reach levels high enough to break longitudinal fibers. The Q-ISO configuration provided an intermediate behavior, with crack originating from the notch and propagating normal to the loading direction, and with a reduction of ultimate tensile strength and strain at failure in comparison to UD specimens. The CONC configuration proved to be effective in shielding the notch area, where no cracks were observed, with the drawback of failure occurring in the central unreinforced area due to fibers straightening towards the outer sides and transversely stretching the matrix in between.

Current stress concentration factor approaches, developed for conventional laminates with homogenized properties, showed to fail capturing the local factors that govern performance for 3D printed composites as these include curved fiber ends, matrix-only notch tips, and local voids [46] created during printing.

Optimizing fiber paths, rather than relying solely on geometry modifications, may significantly improve structural efficiency. Combining unidirectional and contouring deposition algorithms in a hybrid layout should be promising for improving structural performance and prolonging fatigue life. However, further research utilizing multiscale modeling [29,47] or embedded elements techniques [30] and local failure analyses are necessary to fully comprehend failure mechanisms and guide optimal designs.

With enhanced design methods that leverage the complex layouts enabled by 3D printing technologies, additively manufactured notched composite parts have the potential for higher strength, stiffness and fatigue resistance relative to their conventionally manufactured counterparts.

Overall, a shift towards optimizing fiber orientations, rather than geometry, emerges as a promising design strategy for additively manufactured notched composites. But realizing this potential will require overcoming current knowledge gaps through continued basic and applied research that leverages computation, experimentation and multiscale modelling. The results demonstrate progress towards this goal, highlighting critical dependencies and failure modes to inform future optimization efforts.

CRediT authorship contribution statement

Davide Battini: Methodology, Data curation, Visualization, Investigation, Validation, Writing – original draft, Writing – review & editing, Resources. **Luca Giorleo:** Writing – review & editing, Resources. **Andrea Avanzini:** Conceptualization, Methodology, Data curation, Visualization, Investigation, Validation, Writing – original draft, Writing – review & editing, Resources, Supervision.

Declaration of Competing Interest

The authors declare that they have no known competing financial interests or personal relationships that could have appeared to influence the work reported in this paper.

Data availability

Data will be made available on request.

Acknowledgments

Funding: This research did not receive any specific grants from funding agencies in the public, commercial, or not-for-profit sectors.

References

[1] Razavi SMJ, Avanzini A, Cornacchia G, Giorleo L, Berto F. Effect of heat treatment on fatigue behavior of as-built notched Co-Cr-Mo parts produced by Selective Laser Melting. Int J Fatigue 2021;142:105926. https://doi.org/10.1016/j.ijfatigue.2020.105926.

[2] Molaei R, Fatemi A, Phan N. Notched fatigue of additive manufactured metals under axial and multiaxial loadings, part II: Data correlations and life estimations. Int J Fatigue 2022;156:106648. https://doi.org/10.1016/j.ijfatigue.2021.106648.

[3] Maleki E, Bagherifard S, Razavi SMJ, Riccio M, Bandini M, du Plessis A, et al. Fatigue behaviour of notched laser powder bed fusion AlSi10Mg after thermal and mechanical surface post-processing. Mater Sci Eng A 2022;829:142145. https://doi.org/10.1016/j.msea.2021.142145.

[4] Ahmed AA, Susmel L. Static assessment of plain/notched polylactide (PLA) 3D-printed with different infill levels: Equivalent homogenised material concept and Theory of Critical Distances. Fatigue Fract Eng Mater Struct 2019;42:883–904. https://doi.org/10.1111/ffe.12958.

[5] Ahmed AA, Susmel L. A material length scale–based methodology to assess static strength of notched additively manufactured polylactide (PLA). Fatigue Fract Eng Mater Struct 2018;41:2071–98. https://doi.org/10.1111/ffe.12746.

[6] Seibert P, Razavi SMJ, Susmel L, Berto F, Kästner M. Validation of the averaged strain energy density criterion for additively manufactured notched polylactide acid specimens. Procedia Struct Integr 2020;28:2099–103. https://doi.org/10.1016/j.prostr.2020.11.035.

[7] Ng CT, Susmel L. Notch static strength of additively manufactured acrylonitrile butadiene styrene (ABS). Addit Manuf 2020;34:101212. https://doi.org/10.1016/j.addma.2020.101212.

[8] Cicero S, Martínez-Mata V, Alonso-Estebanez A, Castanon-Jano L, Arroyo B. Analysis of notch effect in 3D-printed ABS fracture specimens containing U-notches. Materials (Basel) 2020;13:1–13. https://doi.org/10.3390/ma13214716.

[9] Sánchez M, Cicero S, Arrieta S, Martínez V. Fracture Load Predictions in Additively Manufactured ABS U-Notched Specimens Using Average Strain Energy Density Criteria. Materials (Basel) 2022;15. https://doi.org/10.3390/ma15072372.

[10] Marşavina L, Vălean C, Mărghitaş M, Linul E, Razavi SMJ, Berto F, et al. Effect of the manufacturing parameters on the tensile and fracture properties of FDM 3D-printed PLA specimens. Eng Fract Mech 2022;274. https://doi.org/10.1016/j.engfracmech.2022.108766.

[11] Lorenzo-Bañuelos M, Díaz A, Cuesta II. Influence of raster orientation on the determination of fracture properties of polypropylene thin components produced by additive manufacturing. Theor Appl Fract Mech 2020;107:102536. https://doi.org/10.1016/j.tafmec.2020.102536.

[12] Park SJ, Lee JE, Jin SC, Lee NK, Choi K, Park SH, et al. Tensile test of additively manufactured specimens with external notch removed via laser cutting in material extrusion. Polym Test 2022;110:107581. https://doi.org/10.1016/j.polymertesting.2022.107581.

[13] Crespo M, Gómez-del Río T, Rodríguez J. Failure of polyamide 12 notched samples manufactured by selective laser sintering. J Strain Anal Eng Des 2019;54:192–8. https://doi.org/10.1177/0309324719847817.

[14] Gómez-del Río T, Crespo M, López R, Rodríguez J. Effect of strain rate on tensile fracture behavior of notched polyamide 12 processed by selective laser sintering. Theor Appl Fract Mech 2022;121. https://doi.org/10.1016/j.tafmec.2022.103434.
[15] Avanzini A, Battini D, Pandini S. Static and fatigue behavior in presence of notches for polyamide 12 (PA12) additively manufactured via Multi Jet FusionTM process. Int J Fatigue 2022;161:106912. https://doi.org/10.1016/j.ijfatigue.2022.106912.
[16] Pyl L, Kalteremidou KA, Van Hemelrijck D. Exploration of the design freedom of 3D printed continuous fibre-reinforced polymers in open-hole tensile strength tests. Compos Sci Technol 2019;171:135–51.
[17] Blais P, Toubal L, Zitoune R, Chaib Z. Static and fatigue testing of open-hole and assembled composites based on long carbon fiber and a nylon matrix developed using fused deposition modelling: Multiscale characterization of printed holes and machined holes. Compos Part A Appl Sci Manuf 2022;162:107126.
[18] Suzuki T, Fukushige S, Tsunori M. Load path visualization and fiber trajectory optimization for additive manufacturing of composites. Addit Manuf 2020;31:100942. https://doi.org/10.1016/j.addma.2019.100942.
[19] Khan S, Fayazbakhsh K, Fawaz Z, Arian NM. Curvilinear variable stiffness 3D printing technology for improved open-hole tensile strength. Addit Manuf 2018;24:378–85. https://doi.org/10.1016/j.addma.2018.10.013.
[20] Awerbuch J, Madhukar MS. Notched Strength of Composite Laminates: Predictions and Experiments—A Review. J Reinf Plast Compos 1985;4:3–159. https://doi.org/10.1177/073168448500400102.
[21] Srivastava VK, Kumar D. Prediction of notched strength of laminated fibre composites under tensile loading conditions. J Compos Mater 2002;36:1121–33. https://doi.org/10.1177/0021998302036009581.
[22] Whitney JM, Nuismer RJ. Stress Fracture Criteria for Laminated Composites Containing Stress Concentrations. J Compos Mater 1974;8:253–65. https://doi.org/10.1177/002199837400800303.
[23] Taylor D. On the application of the Theory of Critical Distances for prediction of fracture in fibre composites. Frat Ed Integrità Strutt 2009;4:3–9. https://doi.org/10.3221/igf-esis.11.01.
[24] Morgan D, Quinlan S, Taylor D. Using the theory of critical distances to predict notch effects in fibre composites. Theor Appl Fract Mech 2022;118:103285. https://doi.org/10.1016/j.tafmec.2022.103285.
[25] Ju SH, Chiu CY, Jhao BJ. Determination of V-notch SIFs in multi-material anisotropic wedges by digital correlation experiments. Int J Solids Struct 2010;47:894–900. https://doi.org/10.1016/j.ijsolstr.2009.12.007.
[26] Zappalorto M, Ricotta M. Effect of material orthotropy on the notch stress intensity factors of sharp V-notched plates under tension. Theor Appl Fract Mech 2019;104:102375. https://doi.org/10.1016/j.tafmec.2019.102375.
[27] Torabi AR, Pirhadi E. On the ability of the notch fracture mechanics in predicting the last-ply-failure of blunt V-notched laminated composite specimens: A hard problem can be easily solved by conventional methods. Eng Fract Mech 2019;217:106534. https://doi.org/10.1016/j.engfracmech.2019.106534.
[28] Torabi AR, Pirhadi E. Failure analysis of round-tip V-notched laminated composite plates under mixed mode I/II loading. Theor Appl Fract Mech 2019;104:102342. https://doi.org/10.1016/j.tafmec.2019.102342.
[29] Hoshikawa Y, Shirasu K, Yamamoto K, Hirata Y, Higuchi R, Okabe T. Open-hole tensile properties of 3D-printed continuous carbon-fiber-reinforced thermoplastic laminates: Experimental study and multiscale analysis. J Thermoplast Compos Mater 2022;0:089270572211107. https://doi.org/10.1177/08927057221110791.
[30] Avanzini A, Battini D, Giorleo L. Finite element modelling of 3D printed continuous carbon fiber composites: Embedded elements technique and experimental validation. Compos Struct 2022;292:115631. https://doi.org/10.1016/j.compstruct.2022.115631.
[31] Goh GD, Dikshit V, Nagalingam AP, Goh GL, Agarwala S, Sing SL, et al. Characterization of mechanical properties and fracture mode of additively manufactured carbon fiber and glass fiber reinforced thermoplastics. Mater Des 2018;137:79–89. https://doi.org/10.1016/J.MATDES.2017.10.021.
[32] Lupone F, Padovano E, Venezia C, Badini C. Experimental Characterization and Modeling of 3D Printed Continuous Carbon Fibers Composites with Different Fiber Orientation Produced by FFF Process. Polym 2022, Vol 14, Page 426 2022;14:426. https://doi.org/10.3390/POLYM14030426.
[33] Zhang Z, Yavas D, Liu Q, Wu D. Effect of build orientation and raster pattern on the fracture behavior of carbon fiber reinforced polymer composites fabricated by additive manufacturing. Addit Manuf 2021;47:102204. https://doi.org/10.1016/J.ADDMA.2021.102204.
[34] Lingua A, Piccirelli N, Therriault D, Lévesque M. In-situ full-field measurements for 3D printed polymers during mode I interface failure. Eng Fract Mech 2022;269:108483. https://doi.org/10.1016/J.ENGFRACMECH.2022.108483.
[35] Fernandes RR, Tamijani AY, Al-Haik M. Mechanical characterization of additively manufactured fiber-reinforced composites. Aerosp Sci Technol 2021;113. https://doi.org/10.1016/J.AST.2021.106653.
[36] Prajapati AR, Dave HK, Raval HK. Impact energy absorption and fracture mechanism of FFF made fiberglass reinforced polymer composites. Rapid Prototyp J 2023;29:275–87. https://doi.org/10.1108/RPJ-04-2022-0135/FULL/PDF.
[37] Cheng P, Peng Y, Wang K, Le Duigou A, Yao S, Chen C. Quasi-static penetration property of 3D printed woven-like ramie fiber reinforced biocomposites. Compos Struct 2023;303:116313. https://doi.org/10.1016/J.COMPSTRUCT.2022.116313.
[38] Cheng P, Peng Y, Li S, Rao Y, Le Duigou A, Wang K, et al. 3D printed continuous fiber reinforced composite lightweight structures: A review and outlook. Compos Part B Eng 2023;250:110450. https://doi.org/10.1016/J.COMPOSITESB.2022.110450.
[39] Zappalorto M, Carraro PA. An engineering formula for the stress concentration factor of orthotropic composite plates. Compos Part B Eng 2015;68:51–8. https://doi.org/10.1016/J.COMPOSITESB.2014.08.020.
[40] Jones RM. Mechanics of Composite Materials - 2nd edition, Taylor&Francis Ed. 1999. https://doi.org/10.1115/1.3423688.
[41] Chacón JM, Caminero MA, Núñez PJ, García-Plaza E, García-Moreno I, Reverte JM. Additive manufacturing of continuous fibre reinforced thermoplastic composites using fused deposition modelling: Effect of process parameters on mechanical properties. Compos Sci Technol 2019;181:107688. https://doi.org/10.1016/j.compscitech.2019.107688.
[42] Der Klift F, Van KY, Todoroki A, Ueda M, Hirano Y, Matsuzaki R. 3D Printing of Continuous Carbon Fibre Reinforced Thermo-Plastic (CFRTP) Tensile Test Specimens. Open J Compos Mater 2016;06:18–27. https://doi.org/10.4236/ojcm.2016.61003.
[43] Pascual-González C, Iragi M, Fernández A, Fernández-Blázquez JP, Aretxabaleta L, Lopes CS. An approach to analyse the factors behind the micromechanical response of 3D-printed composites. Compos Part B Eng 2020;186:107820. https://doi.org/10.1016/j.compositesb.2020.107820.
[44] Avanzini A, Petrogalli C, Battini D, Donzella G. Influence of micro-notches on the fatigue strength and crack propagation of unfilled and short carbon fiber reinforced PEEK. Mater Des 2018;139:447–56. https://doi.org/10.1016/j.matdes.2017.11.039.
[45] Young WC, Budynas RG. Stress concentration factors. Roark's Formulas Stress Strain. McGraw Hill 2002:781–2.
[46] Jain A, Kant K, Singh SK, Sahai A, Sharma RS. Process parameter tailored evaluation of FFF-fabricated carbon fibre based poly-lactic-acid composites. J Thermoplast Compos Mater 2023. https://doi.org/10.1177/08927057231155858/ASSET/IMAGES/LARGE/10.1177_08927057231155858-FIG18.JPEG.
[47] Polyzos E, Van Hemelrijck D, Pyl L. Numerical modelling of the elastic properties of 3D-printed specimens of thermoplastic matrix reinforced with continuous fibres. Compos Part B Eng 2021;211:108671. https://doi.org/10.1016/J.COMPOSITESB.2021.108671.